

Verification of Hypervelocity Bulge Red Clump Stars

GABRIELA WOJTKOWSKA¹ AND RADOSŁAW POLESKI¹

¹*Astronomical Observatory, University of Warsaw, Al. Ujazdowskie 4 00-478 Warszawa, Poland*

ABSTRACT

We verify candidate hypervelocity red clump stars located in the Galactic bulge that were selected based on the VVV and the *Gaia* DR2 data by Luna et al. (2019). To do so, we analyze data from the OGLE-IV survey: difference images and astrometric time series. We have data for 30 stars out of 34 hypervelocity candidates. We confirmed high proper motion of only one of these stars and find out that it is a nearby one, hence, not hypervelocity. To sum up, we do not confirm the candidate stars as hypervelocity ones. Hence, we disprove the production rate of hypervelocity red clump stars by the central supermassive black hole provided by Luna et al. (2019).

Keywords: hypervelocity stars — proper motions — Galaxy dynamics

1. INTRODUCTION

Stars with galactocentric velocities higher than the Milky Way escape velocity are called hypervelocity stars (HVSs; see Brown 2015, for a review). At the Sun position the escape velocity is estimated to be around 550 km s^{-1} , though the uncertainty is on the order of 10% (Williams et al. 2017; Monari et al. 2018; Deason et al. 2019). The value changes with a galactocentric distance powered to approximately -0.2 (Williams et al. 2017). The existence of HVSs was first predicted by Hills (1988) who also suggested, that HVSs might be used to prove that there is a supermassive black hole (BH) in the center of the Galaxy. The proof lies in the way HVSs might gain their velocities: if a binary encounters a BH, one of the stars enters the orbit around the BH, while the other one escapes and becomes an HVS. However, this is not the only possible mechanism in which an HVS might be formed. Two other possibilities of HVSs origin were suggested by Yu & Tremaine (2003). The first one is an interaction between two single stars in a dense region close to the Galactic center which results in one of the stars being ejected. The rate of ejected stars becoming an HVS is low ($10^{-11}/\text{yr}$). Another mechanism implies that there is an intermediate-mass BH orbiting around the supermassive BH in the Galactic Center. An interaction between a single star and this BH binary could also result in ejection of an HVS. There are also other theories regarding the HVSs origins, such as ejection from a supernova explosion (Abadi et al. 2009).

The HVSs traveled dozens or hundreds of kpc, even if they are still young. Therefore, they can provide information about the orientation and shape of visible and dark matter in the Galaxy (Marchetti 2021). Such studies can be more detailed if larger samples of HVSs are found. Currently there are around 40 well-established HVSs (Boubert et al. 2018; El-Badry et al. 2023) though there were a number of studies verifying tens or even hundreds of candidates (e.g., Boubert et al. 2018; Li et al. 2021; Marchetti et al. 2019; Ziegerer et al. 2015).

In this paper, we verify HVS candidates presented by Luna et al. (2019), who used the *Gaia* Data Release 2 (DR2; Gaia Collaboration & Brown et al. 2018; Gaia Collaboration et al. 2016) and the VISTA Variables in the Via Lactea Survey (VVV; Minniti et al. 2010; Alonso-García et al. 2018) data to search for such stars toward the Galactic bulge. This search resulted in 34 bulge red clump (RC) stars that have high proper motions (PMs; here we consider $\mu > 100 \text{ mas yr}^{-1}$ as a high PM). The estimated heliocentric distances to these stars are between 6 and 11 kpc, hence, their transverse velocities are larger than the escape velocity at their location. Consequently, these 34 stars were considered candidate hypervelocity RC stars (HVRCs) and if confirmed will almost double the sample of HVSs. Among these candidates, seven stars have PMs pointing away from the Galactic Center. Based on these seven stars, Luna et al. (2019) also estimated the total production rate of HVRCs by the central supermassive BH: $N \approx 3.26 \times 10^{-4} \text{ yr}^{-1}$.

We verify the Luna et al. (2019) candidates by measuring their PMs. Since the stars are relatively faint, for majority of them, the *Gaia* astrometry has poor precision. Furthermore, because all of the stars are in the Bulge region, *Gaia* is not able to collect data about every star every time it is observed, so it is hard to measure PMs. That is why we use the astrometry from the fourth phase of the Optical Gravitational Lensing Experiment (OGLE-IV; Udalski et al. 2015). The OGLE-IV data used here contain hundreds of epochs collected over 8-9 years typically, hence, the PMs can be measured using these data reliably.

The paper is organized as follows: In Section 2 we introduce the methods used by Luna et al. (2019) and a list of the selected targets. We describe the data we used to verify the candidates in Section 3. We present our methods in Section 4 and results in Section 5. These results are discussed in Section 6.

2. TARGET SELECTION

Luna et al. (2019) analyzed the sample of 29,181,380 sources from the Bulge region using the VVV and *Gaia* DR2 data. The sources had to appear in both datasets and have photometry in both near-IR and optical bands. Using the *G*-band magnitude from the *Gaia* DR2 and the *K_s*-band magnitude from the VVV catalog, they created a color-magnitude diagram and selected stars belonging to the RC. Next, they measured PMs using two epochs: one from 2010 and one from 2015. To obtain the PM, the separation of the two centroids was measured and divided by the time difference. Further, they selected stars with high PMs (the limiting value was not indicated but all or almost all selected stars have $\mu > 100 \text{ mas yr}^{-1}$ – see their Tab. 3 and Fig. 2). After that, Luna et al. (2019) excluded nearby sources, defined as having a relative parallax uncertainty smaller than 20% in the *Gaia* DR2. Their research resulted in finding 34 stars with distances between 6 and 11 kpc and high PMs, listed in Table 1.

If HVSs were created by the Hills mechanism, then they should be moving away from the Galactic Center. Therefore, Luna et al. (2019) also selected the sources with tangential velocities meeting this criterion. This selection resulted in a sample of seven stars, presented in Table 2. Among the proper motions of these stars in Luna et al. (2019), the smallest value is $123 \pm 31 \text{ mas yr}^{-1}$. This value should be compared with proper motion expected for a HVS in the Galactic bulge. For example, at a distance of 1 kpc from the Galactic center, the escape velocity would be 840 km s^{-1} . If a star located 8 kpc from Sun has transverse of 840 km s^{-1} , then its proper motion is 21 mas yr^{-1} .

3. OBSERVATIONAL DATA

no.	<i>Gaia</i> DR2 Source ID	<i>G</i> [mag]	R.A. [°]	Dec. [°]	d_{L19} [kpc]
1	4043657695838288768	17.54	268.26982081	-31.75099406	8.89
2	4050119216276193152	16.41	272.29088035	-29.66355549	8.34
3	4050891554627761536	15.83	273.35497285	-28.05909984	7.44
4	4053940195338701056	19.69	265.66792433	-32.97873039	9.06
5	4055694466139424896	17.80	268.30108179	-31.31378523	7.12
6	4055974493662728064	19.41	267.27958008	-30.60787786	7.39
7	4056079565914165760	17.66	268.45517554	-30.94136746	10.28
8	4056243191160985728	16.97	269.92205870	-29.96227506	9.93
9	4056355405826018688	18.76	267.68870103	-30.39436359	7.79
10	4056475218139133568	19.58	267.95180068	-29.38624439	7.39
11	4056562732513987200	17.69	268.39043931	-29.27377801	7.88
12	4056575308188029056	18.19	268.22054632	-29.19157488	7.45
13	4056799093014910848	18.30	266.69167615	-30.17967099	7.90
14	4059583335633235456	18.07	262.45358127	-29.02761085	9.64
15	4060422022558245248	18.66	264.26021020	-28.50495081	7.41
16	4060809836556331648	17.46	266.36967922	-27.13301289	10.08
17	4060841348825794432	18.70	265.09103706	-27.82013489	7.27
18	4060858970977014784	18.91	264.92158105	-27.64125876	7.02
19	4060875566737607936	19.00	265.43546801	-27.52852279	7.32
20	4061174432075039488	18.34	263.21342128	-28.04755677	7.66
21	4061331898466070528	18.39	264.00263015	-26.97930527	8.65
22	4061839842728015360	18.58	265.12969259	-26.23197613	10.71
23	4062483636849326080	16.93	270.11054097	-28.54237150	10.17
24	4063159634713680384	16.78	271.09154633	-27.07320334	8.52
25	4063179906906412032	16.98	270.22075768	-27.37100605	7.85
26	4064174891897213312	19.74	270.35669546	-25.84324584	8.27
27	4064524266009265024	17.24	272.58165108	-26.86186124	8.82
28	4064649163703681792	17.56	273.73570012	-26.34858782	9.92
29	40656397205555867904	18.11	271.47611453	-25.57422902	8.91
30	4066241497024032768	18.12	272.94310441	-24.07029006	7.57
31	4068160003069338112	18.00	265.08148683	-25.13218491	9.67
32	4089677381280701312	16.81	274.84724066	-22.93497132	9.53
33	4110276761609748096	17.75	264.15273504	-24.76831135	8.74
34	4116316451998289664	18.45	264.37354633	-24.29284738	10.75

Table 1. List of 34 HVRCs candidates from Luna et al. (2019). Precise equatorial coordinates are extracted based on the *Gaia* DR2 identifiers. Seven final HVRCs candidates from Luna et al. (2019) are boldfaced in the first column. Distances (6th column) are taken from Luna et al. (2019).

no.	<i>Gaia</i> DR2 Source ID	d_{L19} [kpc]	PM_{L19} [mas/yr]	$v_{T,L19}$ [km/s]
10	4056475218139133568	7.39	209 ± 28	7300
15	4060422022558245248	7.41	270 ± 23	9500
17	4060841348825794432	7.27	171 ± 27	5900
19	4060875566737607936	7.32	186 ± 26	6400
20	4061174432075039488	7.66	493 ± 24	17900
22	4061839842728015360	10.71	156 ± 30	7900
23	4062483636849326080	10.17	123 ± 31	5900

Table 2. Seven final HVRCS candidates selected by Luna et al. (2019). Tangential velocities (last column) are based on PMs and distances from VVV.

To verify the candidates proposed by Luna et al. (2019), we used the *I*-band OGLE-IV astrometric data. The OGLE project started in 1992 with the original primary objective of searching for dark matter using the microlensing technique (Udalski et al. 1993). The project continued with four phases – OGLE-I, OGLE-II, OGLE-III, and OGLE-IV (Udalski et al. 2015), differentiated by the camera and telescope upgrades. OGLE-IV phase started in 2010 and here we analyze data collected till March 2020. Observations are carried out with a 1.3-m telescope at the Las Campanas Observatory in Chile (Udalski et al. 1997). The telescope is equipped with a 32-chip $0.26''$ /pixel mosaic CCD camera. Its field of view is 1.4 deg^2 . The available astrometry has between 500 and 7000 epochs. We transform (x, y) pixel coordinates measured on the individual images to the equatorial coordinates based on the bright stars observed by OGLE-IV and included in the *Gaia* DR3 catalog (Gaia Collaboration et al. 2023). The PM and parallax values provided in the *Gaia* DR3 were used to calculate equatorial coordinates for each stars at each epoch. These coordinates were then used to find the transformation.

Stars no. 6, 13, 24, and 26 were not analyzed, as they are not inside the OGLE-IV footprint or have very small number of epochs. We analyzed remaining 30 stars, which includes all seven stars from Table 2.

We transformed the equatorial coordinates from Table 2 to the pixel scale of the OGLE reference images, using software developed by the OGLE group¹. We then searched the OGLE-IV catalog for nearest matching stars. The separation of equatorial coordinates between OGLE-IV and *Gaia* DR2 for almost all these stars is below 63 mas. The only exception is star no. 34 with a separation of 133 mas (this star is later found to have highest proper motion in this sample). The coordinates are closely matched, hence, we the target stars are identified in the OGLE data securely.

We provide *I*-band brightness of these stars in Table 3. In this sample, 22 stars are brighter than $I = 17 \text{ mag}$ and all are brighter than $I = 18.5 \text{ mag}$. Stars at these brightness limits have standard deviation of the OGLE time-series photometry of $\sigma_I < 0.03 \text{ mag}$ and $\sigma_I < 0.1 \text{ mag}$, respectively (Udalski et al. 2015).

4. METHODS

Below we first present qualitative analysis that is based on difference image analysis (DIA). Then we present quantitative analysis of centroids from point-spread function (PSF) method. The DIA and PSF analysis independently analyse OGLE-IV images.

¹ <http://ogle.astrouw.edu.pl/radec2field.html>

4.1. Qualitative analysis

Our first step in verification of the Luna et al. (2019) HVRCS candidates was inspection of the OGLE-IV difference images. We used the provided *Gaia* IDs and acquired the accurate positions of the targets as well as the stars within the 5 arcsec range from the *Gaia* DR2² and VVV³ catalogs. We present difference images for four of HVRCS candidates in Figure 1. These difference images compare the reference image constructed from the images from the begin of the OGLE-IV with an image taken under good seeing conditions at the end of analyzed time range. In difference images one can see how much the amount of flux changed since the beginning of OGLE-IV observations. If it stays the same, the pixel remains gray. If there were any significant changes, it turns white (more flux) or black (less flux). Therefore, if the star has a high PM, we should see it on the image as a white-black dipole (Eyer & Woźniak 2001).

Star no. 4 is an example of a star located near a very bright star, which is one of the factors that could affect the PM measurement. The image of star no. 8 highlights another possible problem. In the *Gaia* DR2 catalog this star has a nearby companion, while in the VVV catalog the companion is not resolved. If the companion is resolved or not depends on the angular resolution of the telescope and, for ground-based telescopes, the seeing of given image. It is worth mentioning, the companion to the star no. 8 is detected in various surveys. The separation of these two stars in the OGLE-III, OGLE-IV, and *Gaia* DR3 catalogs are 0.55", 0.61", and 0.55", respectively. Most of the difference images looked similar to the one with star no. 10 – there is no sign of the difference in flux coming from the area of the sky in which the star is located. Similarly to the star no. 8, the star no. 10 has a companion at a small separation (0.83", 0.84", and 0.88" based on OGLE-III, OGLE-IV, and *Gaia* DR3, respectively). In our opinion, such nearby companions are the main reason of incorrect PM estimates. Inspection of difference images for all studied stars reveals that only one star has high PM: star no. 34.

4.2. Quantitative analysis

Next, we used the OGLE-IV astrometric time series to quantitatively verify HVRCS candidates. This time series come from the OGLE time-series astrometric database (OGLE-URANUS; Udalski et al. 2024, in prep.). In short, all OGLE images of the Galactic bulge fields with the seeing better than 1.25–1.35 arcsec (depending on stellar density of the field and the number of collected epochs) are reduced with the PSF-fitting software DoPhot (Schechter et al. 1993) to derive precise stellar centroids in these dense fields. We note that DoPhot was already used to extract centroids and measure proper motions by other authors, e.g., Sumi et al. (2004) and Tonry et al. (2012). Each image is divided into subfields covering half of a CCD chip and then these subfields are reduced separately. Centroids are extracted using slowly variable PSF. For each subfield, common stars between the OGLE-IV and a set of *Gaia* DR3 objects are found. After correction of the *Gaia* DR3 positions with the *Gaia* proper motions (to be on the same epoch as the current OGLE frame) the 5th order polynomial transformation of the OGLE current frame and (RA,DEC) of the *Gaia* reference frame is derived. Centroids of all detected on the current OGLE frame objects transformed to the *Gaia* reference frame form the OGLE astrometric time series.

² <https://vizier.u-strasbg.fr/viz-bin/VizieR-3?-source=I/345>

³ <http://horus.roe.ac.uk/vsa/index.html>

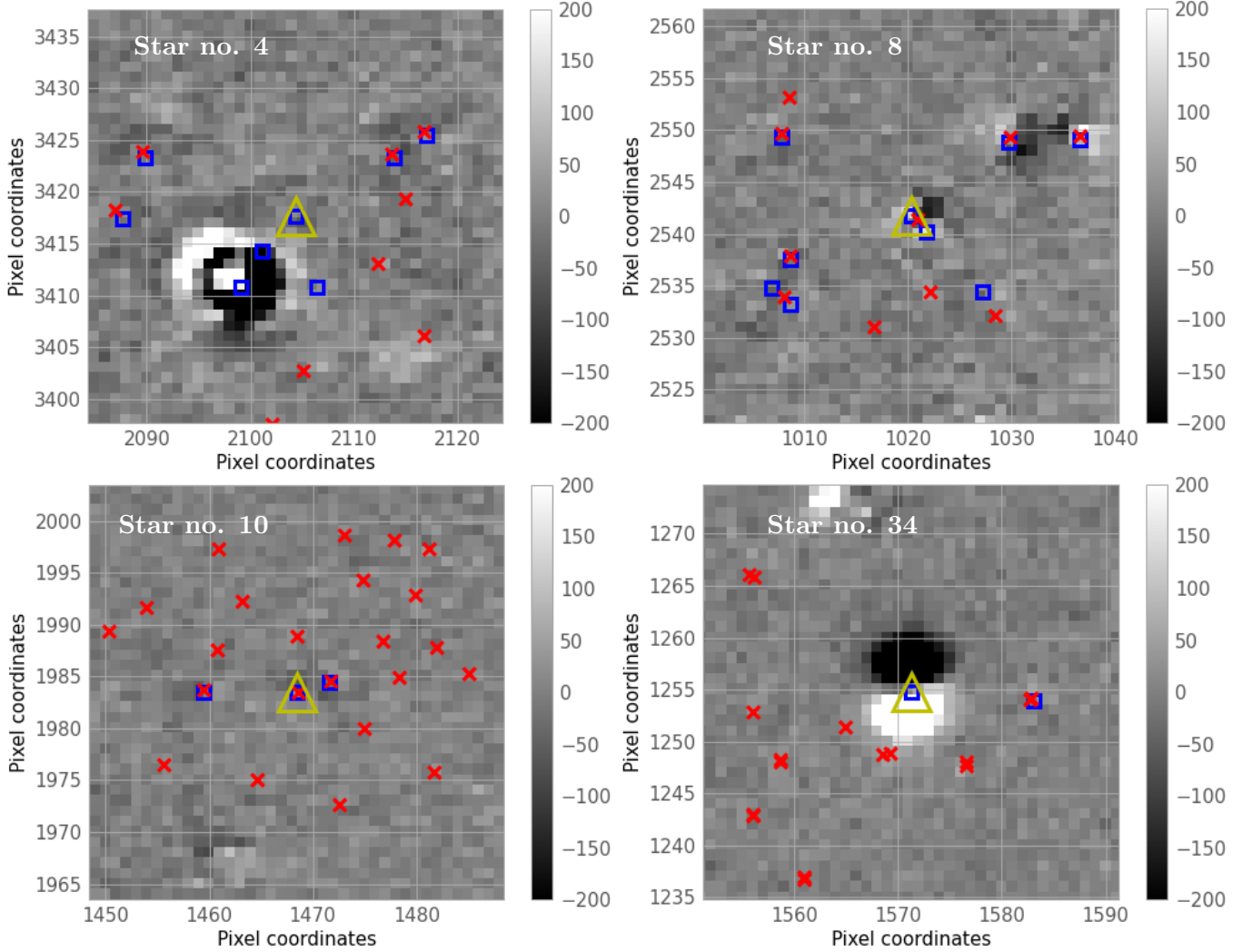


Figure 1. Difference images for stars no. 4, 8, 10, and 34 from the OGLE-IV survey. Both horizontal and vertical axis represent coordinates in pixel scale (1 pixel = 0.26 arcsec). The RA increases toward left and Dec. increases toward top. The color bars plot flux in arbitrary units of the difference images. The target stars are marked with yellow triangles, the coordinates extracted from the *Gaia* DR2 with solid blue squares, and the coordinates extracted from the VVV catalog with red crosses. Lower right panel shows the only high-proper motion star in among 30 verified targets.

We verified the reliability and accuracy of OGLE-URANUS by comparing proper motions to GAIA DR3. We selected stars from the same subfields as 30 targets verified here and limited the sample to the brightness range similar to that of target stars, i.e., $15.3 \text{ mag} < I < 17.4 \text{ mag}$. There were 156,000 stars in this sample and the dispersion of proper motion differences between OGLE-URANUS and GAIA DR3 were 1.7 mas yr^{-1} in the R.A. component and 1.5 mas yr^{-1} in the Dec. component. Hence, OGLE astrometric time-series are accurate enough to verify proper motions presented by Luna et al. (2019).

The astrometric time-series data consist of: right ascension (α), declination (δ), time (t), and seeing (s). We started the investigation by creating graphs visible in Figure 2. The horizontal axis represents

time, and the vertical axes show the right ascension $\Delta\alpha^*$ (upper graph) and the declination $\Delta\delta$ (lower graph). For all of the following images and equations, $\Delta\alpha^*$ is corrected for projection effect:

$$\Delta\alpha^* = \Delta\alpha \cos \delta. \quad (1)$$

The time-series astrometry of the analyzed stars shows outlying measurements which are caused by bad seeing, influence of nearby companion, asteroid etc. For each target star we selected epochs used for fitting based on visual inspection of plots analogous to Figure 2. The epochs used for fitting are between the red horizontal lines.

After that, we calculated the PMs of the stars by fitting a model to the differential astrometry:

$$\Delta\alpha^*(t) = \alpha_0 + \mu_\alpha t + \pi p_\alpha(t), \quad (2)$$

$$\Delta\delta(t) = \delta_0 + \mu_\delta t + \pi p_\delta(t), \quad (3)$$

where π is the parallax, α_0 and δ_0 are the zero-points, μ_α and μ_δ are PMs, and $p_\alpha(t)$ and $p_\delta(t)$ project the parallax unit vector on α and δ directions, respectively.

In order to sample μ_α , μ_δ , and π , we used the Markov Chain Monte Carlo (MCMC) method as implemented by Foreman-Mackey et al. (2013a). We define the likelihood function as:

$$\ln \mathcal{L}(\Delta\delta, \Delta\alpha^* | \mu_\delta, \mu_\alpha, \delta_0, \alpha_0, \pi, f) = -\frac{1}{2} \left(\chi_\alpha^2 + \chi_\delta^2 + \sum_{i=1}^n \ln \sigma_i^2 \right), \quad (4)$$

where

$$\chi_\alpha^2 = \sum_{i=1}^n \left(\frac{\Delta\alpha^*(t_i) - \alpha_0 - \mu_\alpha t_i - \pi p_\alpha(t_i)}{\sigma_i} \right)^2, \quad (5)$$

$$\chi_\delta^2 = \sum_{i=1}^n \left(\frac{\Delta\delta(t_i) - \delta_0 - \mu_\delta t_i - \pi p_\delta(t_i)}{\sigma_i} \right)^2. \quad (6)$$

The uncertainties were obtained by multiplying seeing by a constant (Kuijken & Rich 2002):

$$\sigma_i = f s_i, \quad (7)$$

where f is the fitted multiplication constant.

5. RESULTS

We present the calculated PMs for all the 30 stars in Table 3. Based on these results, only star no. 34 has a high PM. For illustration, we generated the plots showing differential astrometry and fitted models – see Figure 3 for examples. Again, we can see a clear difference between the star with low (star no. 10) and high (star no. 34) PM. We also present the corner plots for the same stars in Figure 4. It is visible, that all of the parameters are independent of each other.

Given all the information gathered, only star no. 34 can be considered a high-PM star. This star was not chosen by Luna et al. (2019) as one of the seven HVRCs moving away from the Galactic Center because of its PM direction. However, this star is not an HVS but a nearby star instead. Luna et al. (2019) did not classify it as a nearby star because its *Gaia* DR2 parallax of 1.03 ± 0.64 mas is consistent with 0. In the *Gaia* DR3 (published after Luna et al. 2019), the parallax is larger and its

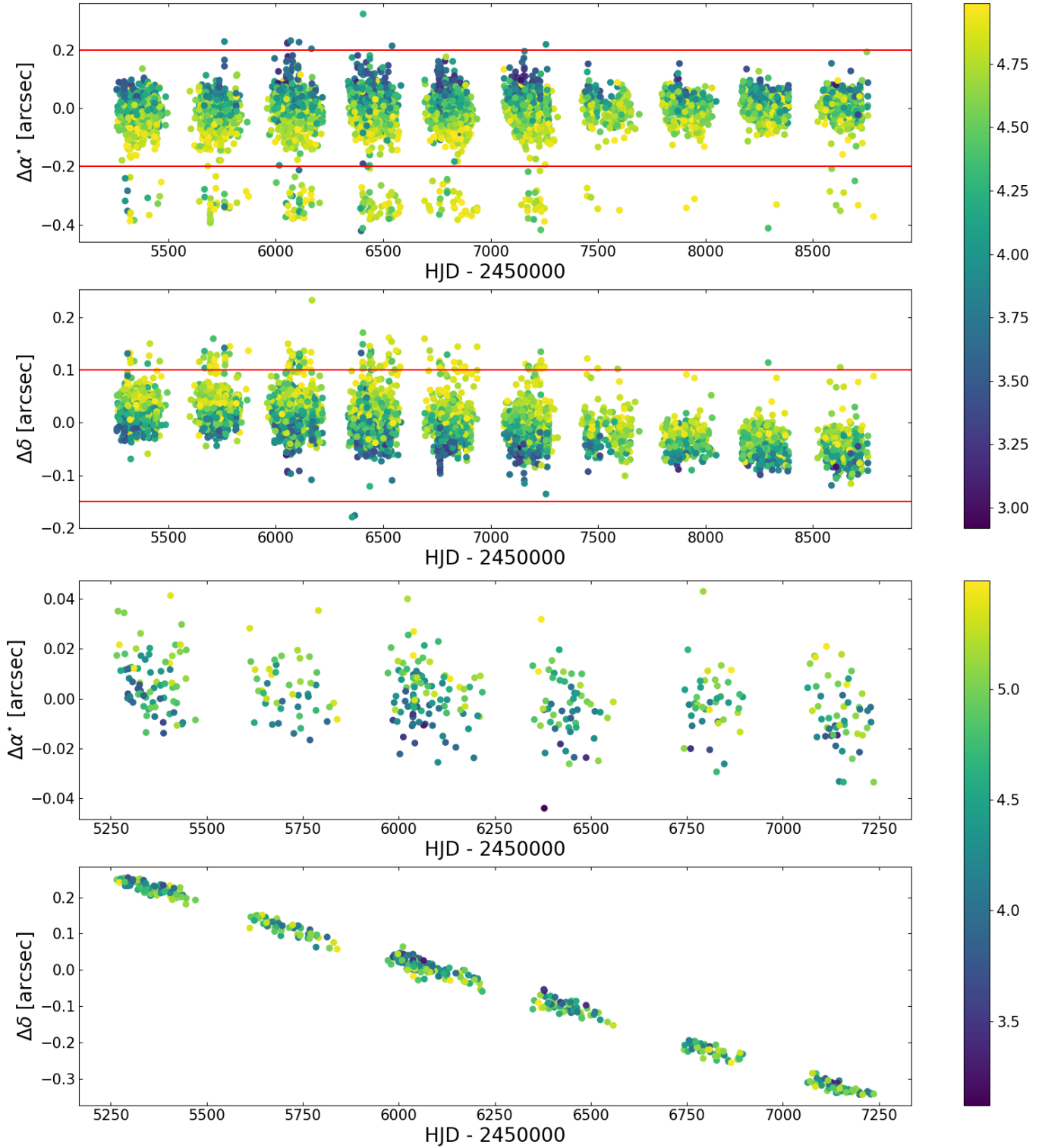


Figure 2. Astrometry of stars no. 10 (top two panels) and 34 (bottom two panels) as a function of time. The Y axes are shifted for plotting purposes. The color-coding indicates seeing (in pixels). The data used for model fitting are between red horizontal lines. For the star no. 34, all data were used for fitting.

uncertainty is smaller: 1.59 ± 0.31 mas (the goodness-of-fit parameter RUWE is 1.477, which is slightly larger than the frequently assumed limit of 1.4). This parallax combined with the photogeometric prior places the star at a distance of 686_{-100}^{+71} pc (Bailer-Jones et al. 2021). One can calculate the transverse velocity by multiplying PM and distance. Our measurement of PM and *Gaia* distance result in transverse velocity of 364_{-53}^{+38} km/s which reveals a star bound to the Galaxy.

Some of the parallax uncertainties in Table 3 are small, hence, we tried to estimate if our data analysis procedures could underestimate the parallax uncertainty. We assumed that the parallax is underestimated by a constant that is added in squares, i.e., $\sigma'_\pi = \sqrt{\sigma_\pi^2 + \epsilon^2}$. We compare the parallaxes and their uncertainties derived from the OGLE-IV astrometry to the distances derived by Bailer-Jones et al. (2021) from the *Gaia* DR3 astrometry and informative priors. The comparison was based on methods presented by Luri et al. (2018) and eight analysed stars which have well-measured *Gaia* data (i.e., goodness-of-fit parameter RUWE smaller than 1.4; these are stars no. 2, 4, 9, 11, 14, 16, 28, and 30). We obtained $\epsilon = 1.77_{-0.48}^{+0.77}$ mas. We note that this value was derived based on a small sample of red clump stars and some of them have nearby companions.

6. DISCUSSION

Our verification does not confirm, that the candidates provided by Luna et al. (2019) are HVSs. Only one of these stars has a high PM but it is a nearby object, not a bulge one, hence, not a hypervelocity one. We analyzed 30 out of 34 HVRCs including all seven stars which Luna et al. (2019) used to estimate the production rate of HVRCs by the central supermassive black hole. Thus, this rate is not supported by any evidence.

In our opinion, the main reason why Luna et al. (2019) results are so different from ours is the approach of Luna et al. (2019) to measure the PMs based on only two epochs. In a very large sample of stars, even a very rare case of measuring one of these positions incorrectly may produce a small sample (about 30 objects in the case discussed here) of stars with high and incorrect PMs. These incorrect measurements of positions are mostly caused by neighboring stars that affect the centroid of the investigated stars.

We note that the tangential velocities calculated by Luna et al. (2019, their Table 3 presented here as Table 2) are extremely large. All of them are at least three times larger than the highest 3D velocity of a well-established HVS (1,755 km/s; Koposov et al. 2020).

We are grateful to the OGLE team (led by A. Udalski) for providing their data. This paper is based on the M.Sc. thesis written by G.W. We thank anonymous reviewer for suggestions that improved the text. We also thank Alonso Luna for comments on a draft. This work has made use of data from the European Space Agency (ESA) mission *Gaia* (<https://www.cosmos.esa.int/gaia>), processed by the *Gaia* Data Processing and Analysis Consortium (DPAC, <https://www.cosmos.esa.int/web/gaia/dpac/consortium>). Funding for the DPAC has been provided by national institutions, in particular the institutions participating in the *Gaia* Multilateral Agreement.

Facilities: 1.3-m Warsaw Telescope at the Las Campanas Observatory, *Gaia* satellite

no.	I [mag]	μ_α [mas/yr]	μ_δ [mas/yr]	π [mas]	f [mas/pixel]
1	16.23	-5.61 ± 0.55	-2.03 ± 0.54	-4.6 ± 2.3	10.92 ± 0.25
2	15.36	-2.10 ± 0.27	-5.32 ± 0.26	-3.1 ± 1.1	5.07 ± 0.12
3	14.78	1.59 ± 0.37	-1.79 ± 0.37	-2.2 ± 1.1	3.62 ± 0.12
4	17.86	0.8 ± 1.2	-2.8 ± 1.3	6.1 ± 5.5	16.41 ± 0.55
5	16.47	-3.087 ± 0.075	0.810 ± 0.074	0.78 ± 0.31	2.815 ± 0.034
7	16.38	-9.21 ± 0.16	-4.25 ± 0.16	5.42 ± 0.66	5.779 ± 0.073
8	15.51	0.88 ± 0.45	-3.65 ± 0.45	-2.0 ± 1.9	11.75 ± 0.20
9	17.26	-1.42 ± 0.17	-5.38 ± 0.18	2.92 ± 0.69	8.503 ± 0.072
10	17.99	2.48 ± 0.27	-8.73 ± 0.27	15.3 ± 1.0	12.80 ± 0.11
11	16.30	1.23 ± 0.31	-1.33 ± 0.32	-0.6 ± 1.2	9.99 ± 0.14
12	16.69	0.77 ± 0.24	-4.04 ± 0.24	-5.1 ± 1.1	8.21 ± 0.11
14	16.74	-3.32 ± 0.44	-8.24 ± 0.44	-5.9 ± 1.9	7.61 ± 0.21
15	17.17	-1.49 ± 0.50	-0.77 ± 0.50	-8.2 ± 1.8	7.72 ± 0.20
16	16.15	-0.23 ± 0.15	0.22 ± 0.14	-0.85 ± 0.65	2.244 ± 0.066
17	17.22	-0.34 ± 0.62	-9.07 ± 0.61	-1.8 ± 2.0	9.85 ± 0.22
18	17.37	-1.1 ± 1.1	-2.4 ± 1.0	-1.5 ± 3.5	12.38 ± 0.41
19	17.53	-1.59 ± 0.69	-8.87 ± 0.69	-7.1 ± 2.2	11.42 ± 0.24
20	16.84	-4.94 ± 0.66	-5.46 ± 0.63	-5.7 ± 2.6	8.84 ± 0.28
21	16.97	-3.11 ± 0.20	-7.35 ± 0.20	9.3 ± 0.8	7.61 ± 0.09
22	18.43	-8.42 ± 0.27	-0.96 ± 0.27	-1.7 ± 1.1	4.03 ± 0.12
23	15.75	-2.34 ± 0.51	-7.13 ± 0.51	-4.1 ± 1.9	10.72 ± 0.20
25	15.67	-2.80 ± 0.18	-5.16 ± 0.17	-1.16 ± 0.75	5.886 ± 0.078
27	15.93	1.16 ± 0.60	-6.04 ± 0.60	-6.5 ± 2.7	8.40 ± 0.27
28	16.16	-2.2 ± 1.0	-5.1 ± 1.0	1.1 ± 4.3	8.04 ± 0.50
29	16.59	-2.70 ± 0.87	-2.61 ± 0.88	0.4 ± 3.5	15.26 ± 0.38
30	16.74	-2.43 ± 0.86	-9.36 ± 0.85	-0.7 ± 2.7	6.00 ± 0.26
31	16.65	-0.2 ± 1.4	-5.4 ± 1.4	-3.7 ± 3.2	6.86 ± 0.36
32	15.42	-6.7 ± 1.6	-7.2 ± 1.6	18.4 ± 5.3	13.42 ± 0.52
33	16.40	-1.4 ± 4.6	-3.9 ± 4.6	26.0 ± 17.0	47.0 ± 1.8
34	16.91	-2.80 ± 0.57	-111.84 ± 0.54	1.8 ± 1.3	3.78 ± 0.14

Table 3. Proper motions, parallaxes, and uncertainty to seeing ratios for the 30 analyzed stars. The second column gives the I -band brightness in the OGLE-IV photometry. The other values are derived from the OGLE-IV time-series astrometry. Seven final HVRCS candidates from Luna et al. (2019) are boldfaced in the first column.

Software: Astropy (Astropy Collaboration et al. 2013, 2018, 2022), corner.py (Foreman-Mackey 2016), DoPhot (Schechter et al. 1993), EMCEE (Foreman-Mackey et al. 2013b), matplotlib (Hunter 2007), numpy (Harris et al. 2020), OGLE databases (Szymanski & Udalski 1993).

REFERENCES

- Abadi, M. G., Navarro, J. F., & Steinmetz, M. 2009, *ApJL*, 691, L63.
<https://arxiv.org/abs/0810.1429>
- Alonso-García, J., Saito, R. K., Hempel, M., et al. 2018, *A&A*, 619, A4.
<https://arxiv.org/abs/1808.06139>

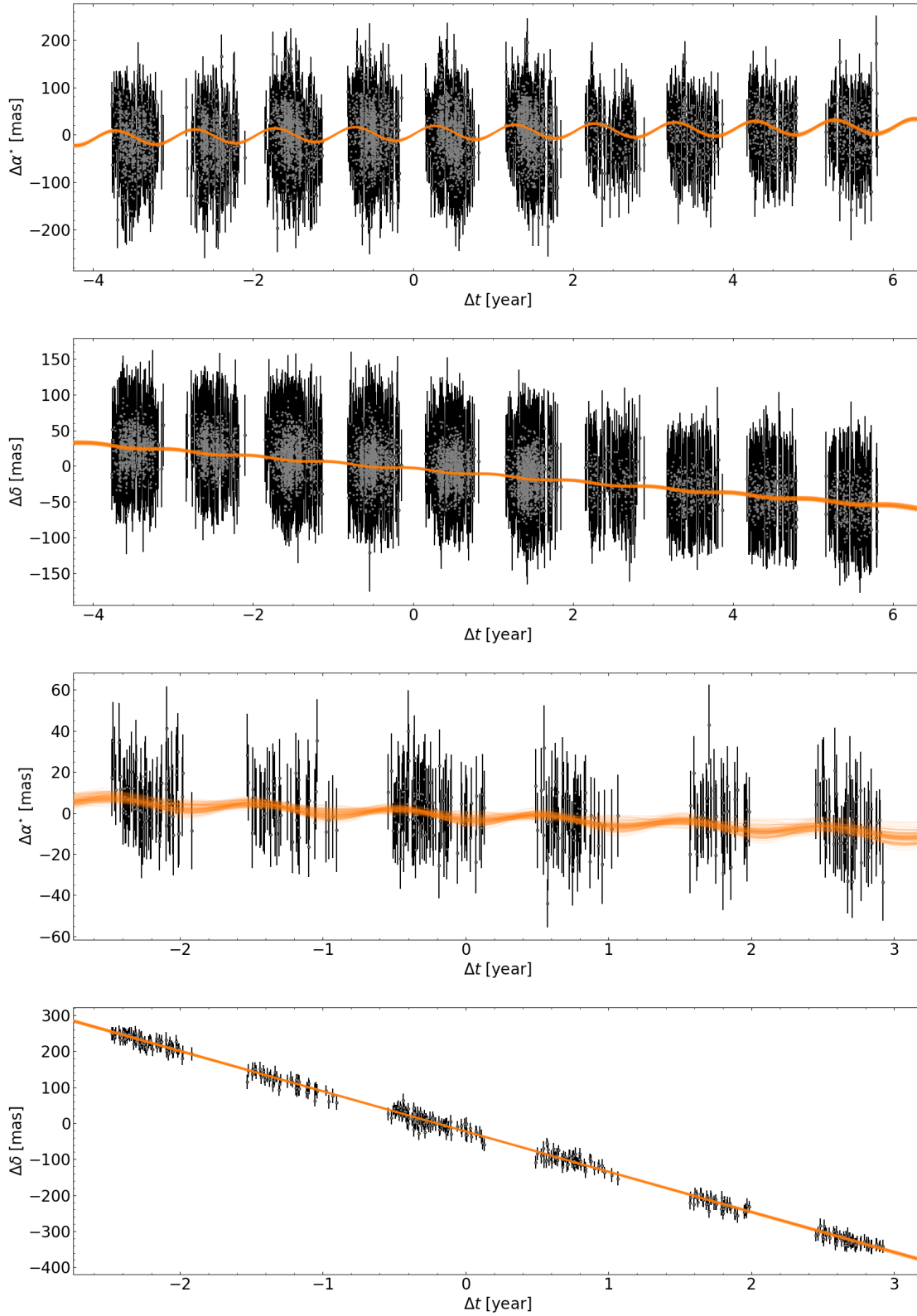


Figure 3. Differential astrometry vs. time with fitted models (orange curves) for stars no. 10 (top) and 34 (bottom).

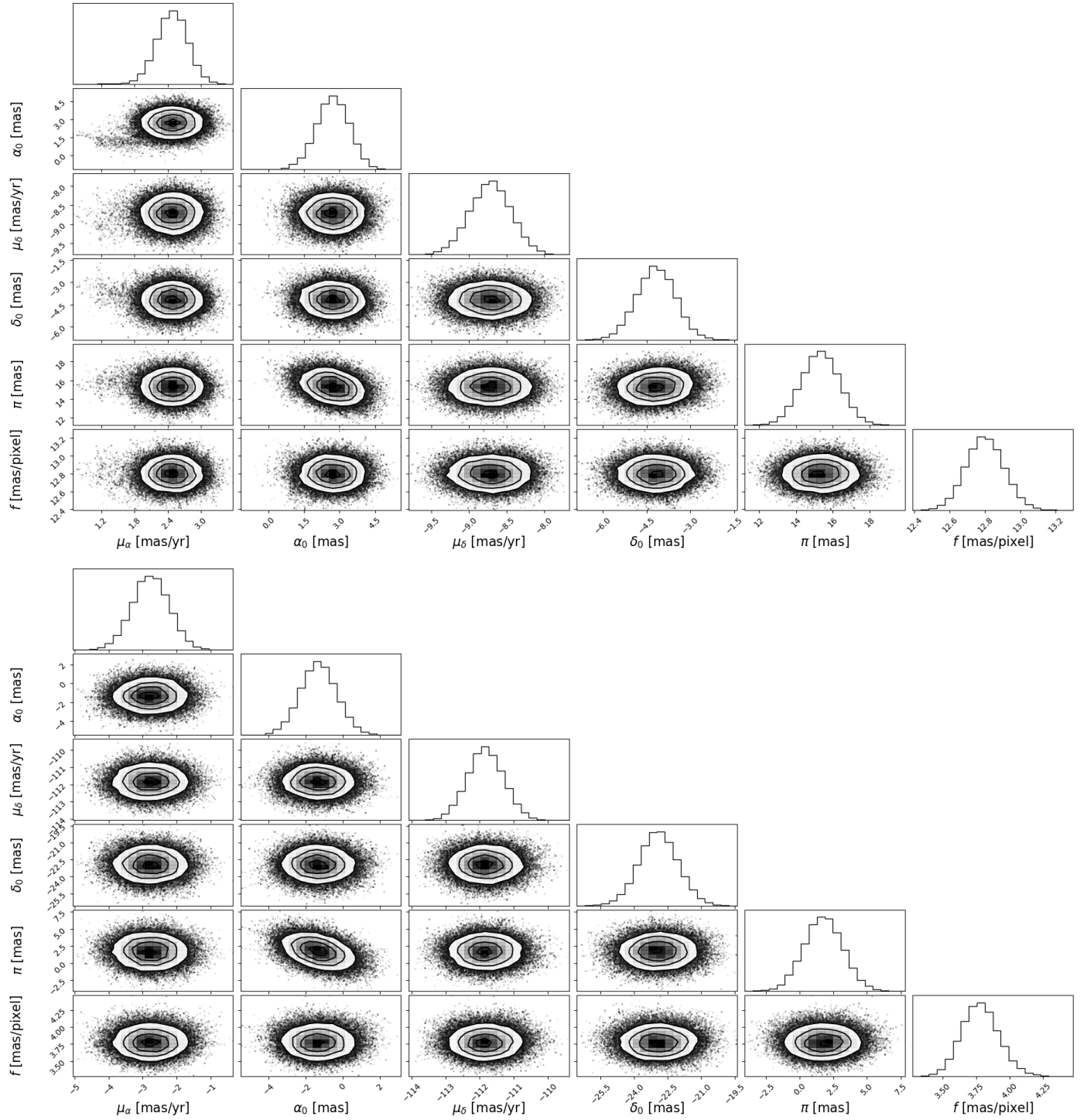


Figure 4. Corner plots of posterior distribution of parameters for stars no. 10 (top) and 34 (bottom).

- Astropy Collaboration, Robitaille, T. P., Tollerud, E. J., et al. 2013, *A&A*, 558, A33, doi: [10.1051/0004-6361/201322068](https://doi.org/10.1051/0004-6361/201322068)
- Astropy Collaboration, Price-Whelan, A. M., Sipőcz, B. M., et al. 2018, *AJ*, 156, 123, doi: [10.3847/1538-3881/aabc4f](https://doi.org/10.3847/1538-3881/aabc4f)
- Astropy Collaboration, Price-Whelan, A. M., Lim, P. L., et al. 2022, *ApJ*, 935, 167, doi: [10.3847/1538-4357/ac7c74](https://doi.org/10.3847/1538-4357/ac7c74)
- Bailer-Jones, C. A. L., Rybizki, J., Fouesneau, M., Demleitner, M., & Andrae, R. 2021, *AJ*, 161, 147, doi: [10.3847/1538-3881/abd806](https://doi.org/10.3847/1538-3881/abd806)
- Boubert, D., Guillochon, J., Hawkins, K., et al. 2018, *MNRAS*, 479, 2789, <https://arxiv.org/abs/1804.10179>
- Brown, W. R. 2015, *ARA&A*, 53, 15, doi: [10.1146/annurev-astro-082214-122230](https://doi.org/10.1146/annurev-astro-082214-122230)
- Deason, A. J., Fattahi, A., Belokurov, V., et al. 2019, *MNRAS*, 485, 3514, doi: [10.1093/mnras/stz623](https://doi.org/10.1093/mnras/stz623)
- El-Badry, K., Shen, K. J., Chandra, V., et al. 2023, *The Open Journal of Astrophysics*, 6, 28, doi: [10.21105/astro.2306.03914](https://doi.org/10.21105/astro.2306.03914)
- Eyer, L., & Woźniak, P. R. 2001, *MNRAS*, 327, 601. <https://arxiv.org/abs/astro-ph/0102027>
- Foreman-Mackey, D. 2016, *The Journal of Open Source Software*, 1, 24, doi: [10.21105/joss.00024](https://doi.org/10.21105/joss.00024)
- Foreman-Mackey, D., Hogg, D. W., Lang, D., & Goodman, J. 2013a, *PASP*, 125, 306, <https://arxiv.org/abs/1202.3665>
- . 2013b, *PASP*, 125, 306, doi: [10.1086/670067](https://doi.org/10.1086/670067)
- Gaia Collaboration, & Brown et al., A. G. A. 2018, *A&A*, 616, A1, <https://arxiv.org/abs/1804.09365>
- Gaia Collaboration, Prusti, T., de Bruijne, J. H. J., et al. 2016, *A&A*, 595, A1, doi: [10.1051/0004-6361/201629272](https://doi.org/10.1051/0004-6361/201629272)
- Gaia Collaboration, Vallenari, A., Brown, A. G. A., et al. 2023, *A&A*, 674, A1, doi: [10.1051/0004-6361/202243940](https://doi.org/10.1051/0004-6361/202243940)
- Harris, C. R., Millman, K. J., van der Walt, S. J., et al. 2020, *Nature*, 585, 357, doi: [10.1038/s41586-020-2649-2](https://doi.org/10.1038/s41586-020-2649-2)
- Hills, J. G. 1988, *Nature*, 331, 687, doi: [10.1038/331687a0](https://doi.org/10.1038/331687a0)
- Hunter, J. D. 2007, *Computing in Science & Engineering*, 9, 90, doi: [10.1109/MCSE.2007.55](https://doi.org/10.1109/MCSE.2007.55)
- Koposov, S. E., Boubert, D., Li, T. S., et al. 2020, *MNRAS*, 491, 2465, <https://arxiv.org/abs/1907.11725>
- Kuijken, K., & Rich, R. M. 2002, *AJ*, 124, 2054, <https://arxiv.org/abs/astro-ph/0207116>
- Li, Y.-B., Luo, A. L., Lu, Y.-J., et al. 2021, *ApJS*, 252, 3, doi: [10.3847/1538-4365/abc16e](https://doi.org/10.3847/1538-4365/abc16e)
- Luna, A., Minniti, D., & Alonso-García, J. 2019, *ApJL*, 887, L39, <https://arxiv.org/abs/1912.02129>
- Luri, X., Brown, A. G. A., Sarro, L. M., et al. 2018, *A&A*, 616, A9, doi: [10.1051/0004-6361/201832964](https://doi.org/10.1051/0004-6361/201832964)
- Marchetti, T. 2021, *MNRAS*, 503, 1374, <https://arxiv.org/abs/2012.02123>
- Marchetti, T., Rossi, E. M., & Brown, A. G. A. 2019, *MNRAS*, 490, 157, doi: [10.1093/mnras/sty2592](https://doi.org/10.1093/mnras/sty2592)
- Minniti, D., Lucas, P. W., Emerson, J. P., et al. 2010, *NewA*, 15, 433, doi: [10.1016/j.newast.2009.12.002](https://doi.org/10.1016/j.newast.2009.12.002)
- Monari, G., Famaey, B., Carrillo, I., et al. 2018, *A&A*, 616, L9, doi: [10.1051/0004-6361/201833748](https://doi.org/10.1051/0004-6361/201833748)
- Schechter, P. L., Mateo, M., & Saha, A. 1993, *PASP*, 105, 1342, doi: [10.1086/133316](https://doi.org/10.1086/133316)
- Sumi, T., Wu, X., Udalski, A., et al. 2004, *MNRAS*, 348, 1439, doi: [10.1111/j.1365-2966.2004.07457.x](https://doi.org/10.1111/j.1365-2966.2004.07457.x)
- Szymanski, M., & Udalski, A. 1993, *AcA*, 43, 91
- Tonry, J. L., Stubbs, C. W., Kilic, M., et al. 2012, *ApJ*, 745, 42, doi: [10.1088/0004-637X/745/1/42](https://doi.org/10.1088/0004-637X/745/1/42)
- Udalski, A., Kubiak, M., & Szymanski, M. 1997, *AcA*, 47, 319, <https://arxiv.org/abs/astro-ph/9710091>
- Udalski, A., Szymanski, M., Kaluzny, J., et al. 1993, *AcA*, 43, 289
- Udalski, A., Szymański, M. K., & Szymański, G. 2015, *AcA*, 65, 1, <https://arxiv.org/abs/1504.05966>
- Williams, A. A., Belokurov, V., Casey, A. R., & Evans, N. W. 2017, *MNRAS*, 468, 2359, doi: [10.1093/mnras/stx508](https://doi.org/10.1093/mnras/stx508)
- Yu, Q., & Tremaine, S. 2003, *ApJ*, 599, 1129, <https://arxiv.org/abs/astro-ph/0309084>
- Ziegerer, E., Volkert, M., Heber, U., et al. 2015, *A&A*, 576, L14, doi: [10.1051/0004-6361/201526052](https://doi.org/10.1051/0004-6361/201526052)